

Journal of Astronomical Telescopes, Instruments, and Systems

AstronomicalTelescopes.SPIEDigitalLibrary.org

In-flight verification of the calibration and performance of the ASTRO-H (Hitomi) Soft X-ray Spectrometer

Maurice A. Leutenegger	Caroline A. Kilbourne	Peter J. Serlemitsos
Marc Audard	Shu Koyama	Hiromi Seta
Kevin R. Boyce	Sho Kurashima	Gary Sneiderman
Gregory V. Brown	Yoshitomo Maeda	Yang Soong
Meng P. Chiao	Maxim Markevitch	Satoshi Sugita
Megan E. Eckart	Dan McCammon	Andrew E. Szymkowiak
Ryuichi Fujimoto	Kazuhisa Mitsuda	Yoh Takei
Akihiro Furuzawa	Hideyuki Mori	Makoto Tashiro
Matteo Guainazzi	Nozomi Nakaniwa	Yuzuru Tawara
Daniel Haas	Takashi Okajima	Masahiro Tsujimoto
Takayuki Hayashi	Stéphane Paltani	Cor P. de Vries
Jan-Willem den Herder	Robert Petre	Tomomi Watanabe
Ryo Iizuka	F. Scott Porter	Shinya Yamada
Manabu Ishida	Kosuke Sato	Noriko Yamasaki
Yoshitaka Ishisaki	Toshiki Sato	
Naomichi Kikuchi	Makoto Sawada	

Maurice A. Leutenegger, Marc Audard, Kevin R. Boyce, Gregory V. Brown, Meng P. Chiao, Megan E. Eckart, Ryuichi Fujimoto, Akihiro Furuzawa, Matteo Guainazzi, Daniel Haas, Takayuki Hayashi, Jan-Willem den Herder, Ryo Iizuka, Manabu Ishida, Yoshitaka Ishisaki, Naomichi Kikuchi, Caroline A. Kilbourne, Shu Koyama, Sho Kurashima, Yoshitomo Maeda, Maxim Markevitch, Dan McCammon, Kazuhisa Mitsuda, Hideyuki Mori, Nozomi Nakaniwa, Takashi Okajima, Stéphane Paltani, Robert Petre, F. Scott Porter, Kosuke Sato, Toshiki Sato, Makoto Sawada, Peter J. Serlemitsos, Hiromi Seta, Gary Sneiderman, Yang Soong, Satoshi Sugita, Andrew E. Szymkowiak, Yoh Takei, Makoto Tashiro, Yuzuru Tawara, Masahiro Tsujimoto, Cor P. de Vries, Tomomi Watanabe, Shinya Yamada, Noriko Yamasaki, "In-flight verification of the calibration and performance of the ASTRO-H (Hitomi) Soft X-ray Spectrometer," *J. Astron. Telesc. Instrum. Syst.* **4**(2), 021407 (2018), doi: 10.1117/1.JATIS.4.2.021407.

In-flight verification of the calibration and performance of the ASTRO-H (Hitomi) Soft X-ray Spectrometer

Maurice A. Leutenegger,^{a,b,*} Marc Audard,^c Kevin R. Boyce,^a Gregory V. Brown,^d Meng P. Chiao,^{a,b,e} Megan E. Eckart,^a Ryuichi Fujimoto,^f Akihiro Furuzawa,^{g,h} Matteo Guainazzi,^{i,j} Daniel Haas,^k Takayuki Hayashi,^{a,g} Jan-Willem den Herder,^k Ryo Iizuka,ⁱ Manabu Ishida,ⁱ Yoshitaka Ishisaki,ⁱ Naomichi Kikuchi,ⁱ Caroline A. Kilbourne,^a Shu Koyama,ⁱ Sho Kurashima,ⁱ Yoshitomo Maeda,ⁱ Maxim Markevitch,^a Dan McCammon,^m Kazuhisa Mitsuda,ⁱ Hideyuki Mori,^a Nozomi Nakaniwa,ⁱ Takashi Okajima,^a Stéphane Paltani,^c Robert Petre,^a F. Scott Porter,^a Kosuke Sato,ⁿ Toshiaki Sato,ⁱ Makoto Sawada,^o Peter J. Serlemitsos,^a Hiromi Seta,ⁱ Gary Sneiderman,^a Yang Soong,^a Satoshi Sugita,^p Andrew E. Szymkowiak,^q Yoh Takei,ⁱ Makoto Tashiro,^r Yuzuru Tawara,^g Masahiro Tsujimoto,ⁱ Cor P. de Vries,^k Tomomi Watanabe,^a Shinya Yamada,ⁱ and Noriko Yamasakiⁱ

^aNASA, Goddard Space Flight Center, Greenbelt, Maryland, United States

^bUniversity of Maryland, Baltimore County, Center for Space Sciences and Technology, Center for Research and Exploration in Space Science and Technology, Baltimore, Maryland, United States

^cUniversity of Geneva, Astronomy Department, Geneva, Switzerland

^dLawrence Livermore National Laboratory, Physics Division, Livermore, California, United States

^eAlcyon Technical Services, Greenbelt, Maryland, United States

^fKanazawa University, Faculty of Mathematics and Physics, Kanazawa, Japan

^gNagoya University, Physics Department, Nagoya, Japan

^hFujita Health University, Physics Division, Nagoya, Japan

ⁱInstitute of Space and Astronautical Science, Department of Space Astronomy and Astrophysics, Sagami-hara, Japan

^jEuropean Space Research and Technology Centre/European Space Agency, Noordwijk, The Netherlands

^kNetherlands Institute for Space Research, Utrecht, The Netherlands

^lTokyo Metropolitan University, Department of Physics, Hachioji, Japan

^mUniversity of Wisconsin, Department of Physics, Madison, Wisconsin, United States

ⁿTokyo University of Science, Department of Physics, Tokyo, Japan

^oAoyama Gakuin University, Department of Physics and Mathematics, Tokyo, Japan

^pTokyo Institute of Technology, Department of Physics, Tokyo, Japan

^qYale University, Department of Physics, New Haven, Connecticut, United States

^rSaitama University, Department of Physics, Saitama, Japan

Abstract. The Soft X-ray Spectrometer onboard the Astro-H (Hitomi) orbiting x-ray observatory featured an array of 36 silicon thermistor x-ray calorimeters optimized to perform high spectral resolution x-ray imaging spectroscopy of astrophysical sources in the 0.3- to 12-keV band. Extensive preflight calibration measurements are the basis for our modeling of the pulse height–energy relation and energy resolution for each pixel and event grade, telescope collecting area, detector efficiency, and pulse arrival time. Because of the early termination of mission operations, we needed to extract the maximum information from observations performed only days into the mission when the onboard calibration sources had not yet been commissioned and the dewar was still coming into thermal equilibrium, so our technique for reconstructing the per-pixel time-dependent pulse height–energy relation had to be modified. The gain scale was reconstructed using a combination of an absolute energy scale calibration at a single time using a fiducial from an onboard radioactive source and calibration of a dominant time-dependent gain drift component using a dedicated calibration pixel, as well as a residual time-dependent variation using spectra from the Perseus cluster of galaxies. The energy resolution was also measured using the onboard radioactive sources. It is consistent with instrument-level measurements accounting for the modest increase in noise due to spacecraft systems interference. We use observations of two pulsar wind nebulae to validate our models of the telescope area and detector efficiency and to derive a more accurate value for the thickness of the gate-valve Be window, which had not been opened by the time mission operations ceased. We use observations of the Crab nebula to refine the pixel-to-pixel timing and validate the absolute timing. © The Authors. Published by SPIE under a Creative Commons Attribution 3.0 Unported License.

Distribution or reproduction of this work in whole or in part requires full attribution of the original publication, including its DOI. [DOI: [10.1117/1.JATIS.4.2.021407](https://doi.org/10.1117/1.JATIS.4.2.021407)]

Keyword: x-ray calorimeter.

Paper 17062SSP received Aug. 16, 2017; accepted for publication Feb. 22, 2018; published online Mar. 19, 2018.

1 Introduction

The Astro-H (Hitomi)¹ Soft X-ray Spectrometer (SXS)² was designed for high-resolution broadband imaging x-ray spectroscopy with a high effective area. The detector^{3–6} and its cryogenic systems^{7–13} are described in a number of papers,

*Address all correspondence to: Maurice A. Leutenegger, E-mail: maurice.a.leutenegger@nasa.gov

as is the Soft X-ray Telescope (SXT),^{14,15} the on-orbit operation of the instrument,¹⁶ and the data analysis software and archive.¹⁷ The detector¹⁸ and telescope^{19–25} were the subjects of intensive ground calibration campaigns at the subsystem and instrument level. The ground calibration measurements were used to predict the on-orbit performance of the instrument, including the effective area and energy resolution. The ground calibration measurements also were used to derive a calibration for assignment of photon energies to events based on the measured pulse heights and to assign absolute photon arrival times based on the nominal trigger times.

The instrument calibration must be validated and corrected based on on-orbit calibration measurements. The suite of on-board diagnostics included an “always-on” collimated radioactive ⁵⁵Fe source illuminating a calibration pixel installed outside the telescope field of view, an ⁵⁵Fe source installed on a rotatable filter wheel above the SXS dewar aperture, and an electron impact x-ray generator with a photocathode activated by a fast UV photodiode [modulated x-ray source (MXS)]. An extensive set of observations of celestial sources was planned to complement diagnostics from these onboard sources. Because of the unfortunate loss of the observatory during the commissioning phase, only a subset of the planned calibration experiments was carried out. Nevertheless, the instrument performance was largely verified by the data that were collected.

The observations performed in the commissioning phase were not initially planned to be fully calibrated, but because of the loss of the observatory, there is a mandate to extract the maximum possible science return from them. The most important additional requirement introduced by this mandate is a procedure for calibrating the pulse height–energy relation early in the mission, when we performed SXS science observations before fiducial calibration sources were available and while the SXS dewar was still coming into thermal equilibrium. The transmission of the SXS dewar gate valve also had to be calibrated more precisely than the available preflight data allowed.

In this article, we give an overview of four key aspects of the instrument calibration and the on-orbit measurements and observations that were used to validate and/or measure these parameters. In Sec. 2, we describe measurements of the instrument resolution and line spread function (LSF). In Sec. 3, we describe the procedure used to establish the pulse height–energy relation. In Sec. 4, we use observations of bright continuum sources to measure the thickness of Be in the SXS dewar gate valve. In Sec. 5, we use observations of the Crab nebula to make corrections to the absolute and relative event timing.

The on-orbit calibration of the SXS is described in greater depth in a series of forthcoming articles: the LSF is discussed by Leutenegger et al.,²⁶ the pulse height–energy relation is discussed by Eckart et al.,²⁷ the effective area is discussed by Tsujimoto et al.,²⁸ and timing is discussed by Koyama et al.²⁹ Two further articles will describe topics not covered here: the SXS background is discussed by Kilbourne et al.³⁰ and the SXT point spread function is discussed by Maeda et al.³¹

2 Line Spread Function

The LSF was characterized on the ground using monochromatic x-ray sources augmented by x-ray fluorescence sources emitting characteristic lines. The LSF is well-characterized by a dominant component consisting of a Gaussian with energy-dependent resolution (the “core” LSF), as well as three weak components (the “extended” LSF): an exponential tail with

e -folding of ~ 12 eV, an electron loss continuum, and escape peaks.¹⁸ The extended LSF components are not expected to vary on orbit, so we do not discuss them further in this article.

The core LSF energy resolution is a function of event grade and pixel. The event grades are described in detail by Ishisaki et al.⁶ To summarize briefly, events are processed differently depending on their relative arrival time, and the method of processing affects the energy resolution for that event type. The classifications are hi-res, mid-res, and low-res; and within mid-res and low-res, events can be primary (first in a series) or secondary (subsequent events in a series). Both preflight and in-flight calibrations of the core LSF are only valid for primary event grades, and a modeling of secondary event grades will be discussed in a future article.

The so-called “baseline” events are a key tool in modeling the energy resolution of the SXS. These events measure the effects of baseline noise in the detector system by processing strings of samples from the outputs in the absence of an x-ray absorption event using the optimally filtered template pulse as if a real event had been triggered. They provide the resolution at zero pulse height, as well as an estimate of all fast time scale noise contributions to the energy resolution.

We have found that the energy resolution for a given event grade and pixel can be modeled as an excess broadening term added in quadrature with the baseline energy resolution

$$\mathcal{R}(E) = \sqrt{\mathcal{R}_b^2 + \mathcal{R}_e^2(E)}, \quad (1)$$

where $\mathcal{R}(E)$ is the energy resolution, \mathcal{R}_b is the baseline energy resolution, and \mathcal{R}_e is the excess broadening. We showed in our preflight calibration campaign that the excess broadening scales linearly with energy, so that

$$\mathcal{R}(E) = \sqrt{\mathcal{R}_b^2 + \mathcal{R}_e^2(E_{\text{ref}}) \left(\frac{E}{E_{\text{ref}}}\right)^2}. \quad (2)$$

In Fig. 1(a), we show the energy resolution for a single pixel measured at several energies in instrument-level testing together with the best-fit model for resolution as a function of energy (discussed in more detail by Eckart et al.¹⁸) and compare this with on-orbit measurements using the ⁵⁵Fe source installed in the filter wheel. In Fig. 1(b), we show the baseline resolution, hi-res event resolution at 5.9 keV, and excess broadening at 5.9 keV for all pixels, comparing measurements from instrument-level testing on the ground with on-orbit measurements using the ⁵⁵Fe source installed in the filter wheel.

We find that the baseline resolution is slightly higher on-orbit compared with instrument-level testing, by an average of 0.38 eV. At least some degradation in resolution is expected, given the noise tones observed due to spacecraft interference from the attitude and orbit control system (AOCS) (see Fig. 7 in the work by Porter et al.³). Noise tones generated by operation of the AOCS in ground testing also led to a degradation in baseline resolution.¹⁸ Note that although the effect of noise tones can be mitigated by creating a new optimal filter based on the changed noise environment, this method cannot be used here because the noise is nonstationary in frequency space; furthermore, changing the optimal filter would invalidate the ground calibration of the gain scale, which would then have to be recalibrated on orbit. In addition to the spacecraft interference, the baseline resolution is further degraded by the presence

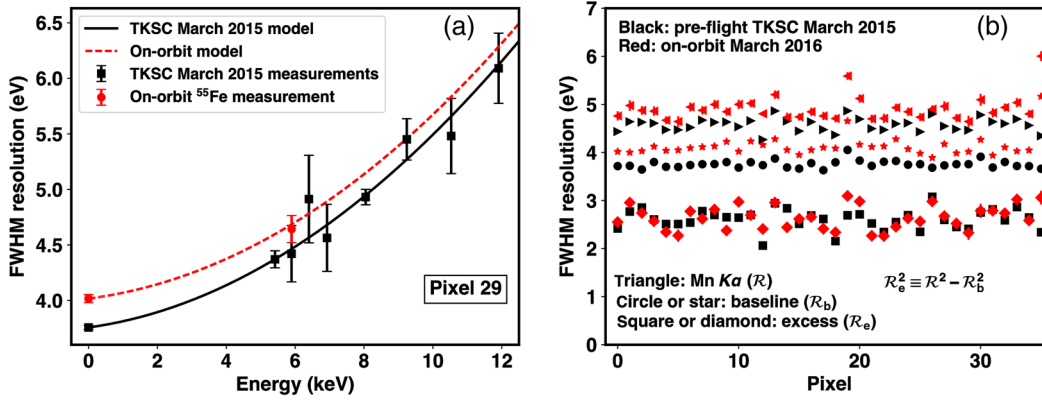


Fig. 1 (a) The black square points and black solid line show the measurements and model from instrument-level testing at TKSC for the energy resolution as a function of energy for hi-res events on pixel 29. The red circle points show the on-orbit measurements using the ^{55}Fe filter wheel source, and the red dashed line shows a model derived from the instrument-level tests modified by the larger baseline resolution experienced in flight. (b) Comparison of the energy resolution at 5.9 keV for hi-res events (triangles: point right, TKSC; point left, on-orbit), baseline resolution (circles, TKSC; stars, on-orbit), and excess broadening at 5.9 keV (squares, TKSC; stars, on-orbit) predicted from the model derived from instrument-level testing (black) at TKSC, and measured on-orbit using the ^{55}Fe filter wheel source exposure (red). Note that pixel 12 is the calibration pixel.

of untriggered thermal crosstalk events resulting from so-called frame events, where minimum ionizing particles deposit energy into the silicon frame. This effect results in a slight degradation in resolution, with the magnitude of the effect dependent on the cutoff rigidity, which is a proxy for the rate of minimum ionizing particles.²⁶

We also find that although the baseline resolution is slightly degraded by operation of the AOCS and the untriggered thermal crosstalk from frame events, the excess broadening at Mn $K\alpha$ averaged over all main array pixels is statistically consistent with that observed in instrument-level testing. We thus conclude that within the statistical sensitivity of our measurements, the on-orbit resolution can be modeled by modifying the preflight model of resolution using the on-orbit baseline resolution [shown as the red curve in Fig. 1(a)]. The one exception to this is the calibration pixel, which has accumulated many more counts than the main array. The calibration pixel shows both increased baseline noise and a small but statistically significant (3σ) increase in the excess broadening from 2.06 ± 0.10 to 2.41 ± 0.08 eV at Mn $K\alpha$. The mechanisms responsible for the increase in excess broadening in the calibration pixel will be investigated in a future article.²⁶

We intended to operate the pulse shape processor (PSP) in “forced mid-res mode,” where all hi-res and mid-res triggered events would be processed with a short pulse template appropriate for mid-res events, allowing calibration of mid-res event gain and energy resolution without having to choose a source count rate that would generate a high fraction of true mid-res events, and also giving a measurement of the mid-res baseline energy resolution. Since this experiment was not completed before the end of mission operations, we instead analyzed the small number of mid-res events accumulated in the ^{55}Fe exposure. We found that the mean resolution was slightly higher than in instrument-level testing, just as for hi-res events. We assumed that the excess broadening for mid-res events was the same in flight as in instrument-level testing, as we found for hi-res events.

For the sake of brevity, in this paragraph, all discussion implicitly pertains to mid-res events. Since we had no on-orbit measurement of the baseline energy resolution, we subtracted

the mean excess broadening (averaged over all pixels) at 5.9 keV that was measured in preflight calibration from the mean energy resolution measured in in-flight at 5.9 keV to obtain an estimate of the mean baseline energy resolution

$$\overline{\mathcal{R}}_{b,o}^2 = \overline{\mathcal{R}}_o^2 - \overline{\mathcal{R}}_{e,g}^2, \quad (3)$$

where the subscript b refers to baseline resolution, e refers to excess broadening, g refers to ground calibration measurements based on data from instrument-level tests at Tsukuba Space Center (TKSC), and o refers to on-orbit measurements. We then took the ratio of the estimated in-flight mean baseline energy resolution to the preflight value to estimate the typical degradation in the baseline resolution, and we used this ratio to rescale the preflight baseline resolution as an estimate of the on-orbit baseline resolution

$$\mathcal{R}_{b,o} = \mathcal{R}_{b,g} \frac{\overline{\mathcal{R}}_{b,o}}{\overline{\mathcal{R}}_{b,g}}. \quad (4)$$

Finally, we computed a new estimated energy resolution as a function of energy using the preflight excess broadening

$$\mathcal{R}_o^2 = \mathcal{R}_{b,o}^2 + \mathcal{R}_{e,g}^2. \quad (5)$$

The calibration of low-res events can be accomplished using the low-res pulse height of any events, which is telemetered for all event grades. We, thus, analyzed the low-res pulse heights of hi-res events in the ^{55}Fe filter wheel exposure to measure the energy resolution at Mn $K\alpha$. We then used these measurements to scale up the preflight model of the low-res energy resolution, under the assumption that the excess broadening was identical, and that the energy resolution at Mn $K\alpha$ increased due to a larger baseline resolution.

3 Gain Scale

The SXS pulse height–energy relation (or gain scale) is crucial in allowing accurate absolute measurements of photon energy. Because the SXS sensors are extremely sensitive thermometers,

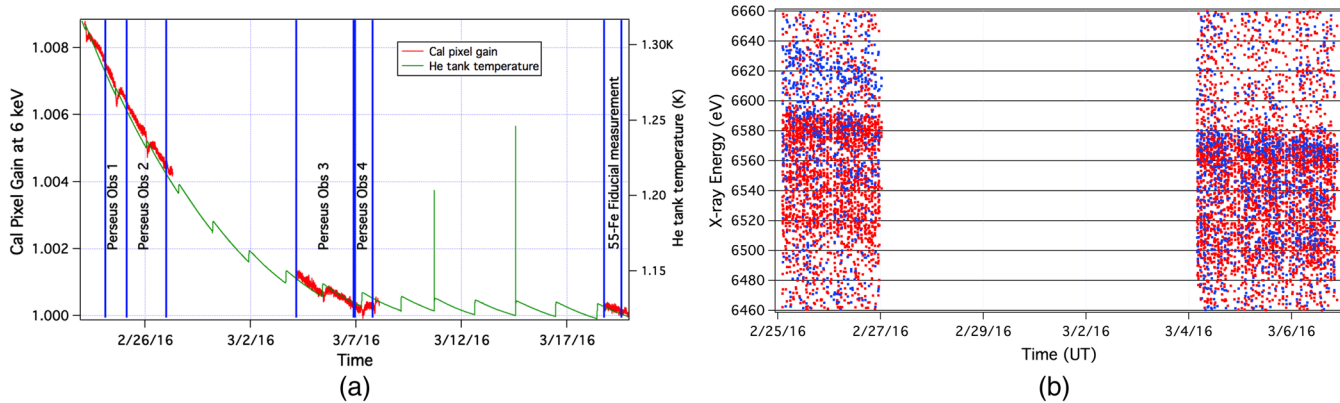


Fig. 2 (a) Gain variation measured with the calibration pixel compared with the He tank temperature. The calibration pixel gain is with respect to reference measurements in instrument-level calibration with a calorimeter thermal sink (CTS) control temperature of 50 mK. (b) Single pixel scatter plot of events recorded in two observations of the Perseus cluster showing photon energy as a function of time. The blue points show the energies calculated using the gain scale derived during ground calibration, uncorrected for any drift, while the red points show the energies after correction for the calibration pixel gain drift. Residual drift is still present, and the absolute energy scale is not fully uncalibrated. The data shown correspond to observations 2 and 3 in panel (a).

the gain scale is very sensitive to the SXS thermal environment. Differential thermal loads between the SXS pixels and the adiabatic demagnetization refrigerator (ADR) control thermometer can lead to substantial gain drift even while nominally controlling the instrument at a constant temperature, and differential thermal loads among pixels can result in differential gain drift among pixels.

An extensive campaign of ground calibration created a solid foundation for understanding and measuring gain scales and gain drift in the SXS.^{18,32} We found that the gain scale for a given stable set of conditions can be well fit with a fourth-order polynomial. We also found that although the polynomial would be different for a different set of thermal conditions, essentially all variation in gain scale can be treated as a variation in the effective temperature of the sensor, which is biased to operate at ~ 10 mK above the 50-mK stage control thermometer. By measuring gain curves at discrete temperature setpoints on the ADR control thermometer while maintaining constant thermal boundary conditions at the other thermal interfaces, we are able to map the change in shape of the gain curve as a function of control temperature. (The most important thermal interfaces affecting the detector effective temperature are the He tank and the inner vapor cooled shield. The SXS cryogenic design is discussed by Fujimoto et al.¹²) We can then interpolate these gain curves for any control temperature setpoint within the range we sampled. When the thermal boundary conditions change, we can measure the gain offset at a single fiducial energy and use this to find an effective temperature (and accompanying gain curve) corresponding to the equivalent control thermometer temperature for the thermal boundary conditions under which the reference gain curves were measured.

The SXS in-flight calibration plan envisioned a threefold approach to measuring and validating the gain scale and monitoring the gain drift. First, a calibration pixel is located outside the instrument field of view and is illuminated by an always-on collimated ^{55}Fe radioactive x-ray source. This allows for continuous monitoring of short-term gain drift, where all pixels are expected to drift in parallel. Second, onboard x-ray sources are available to illuminate the whole SXS array with photons of known energy. These sources include an ^{55}Fe source mounted

on the SXS filter wheel, four MXSs, electron impact sources using fast photocathodes modulated with UV photodiodes. Third, a number of celestial sources featuring emission lines with known energies were planned to be observed, allowing validation of the gain scale across the SXS science band.

Because of the untimely loss of the mission, the SXS gain was not fully validated as planned. Furthermore, the observations of the Perseus cluster during the commissioning phase of the instrument needed to be calibrated as well as possible in order to extract the maximum possible science. Because these observations occurred without contemporaneous full-array gain drift monitoring, accurate calibration of the gain scale required the development of techniques beyond what was intended for standard operation of the SXS.

In Fig. 2(a), we show the calibration pixel gain with respect to the fiducial gain measured in ground calibration as a function of time, together with the He tank temperature. The calibration pixel gain qualitatively tracks the overall trends in the He tank temperature. Other SXS dewar internal temperatures (not shown) correlate to a lesser degree with the gain drift on the calibration pixel and other pixels.

The main array pixels show a qualitatively similar drift to the calibration pixel. We thus measure the calibration pixel gain and remove this “common-mode” gain drift from the whole array as a linear stretch correction applied to the ground calibration curves. Minor modifications to this procedure were adopted in the final pipeline processing for observations beginning with Perseus Obs 3. These changes will be motivated and explained by Eckart et al.²⁷ Figure 2(b) shows a scatter plot of event energies in the Fe xxv complex for observations of the Perseus cluster using a single pixel after applying this correction based on the calibration pixel. Significant gain drift is still visible, both between the observations, which are separated by 6 days, and even within the observations, especially the earlier one, when dewar internal interface temperatures are more rapidly drifting. We term the residual gain drift as “differential” gain drift, both because it is differential relative to the calibration pixel but also between the different pixels of the main array.

We can quantify the differential gain drift for a given pixel at any point by fitting an empirical model composed of a series of

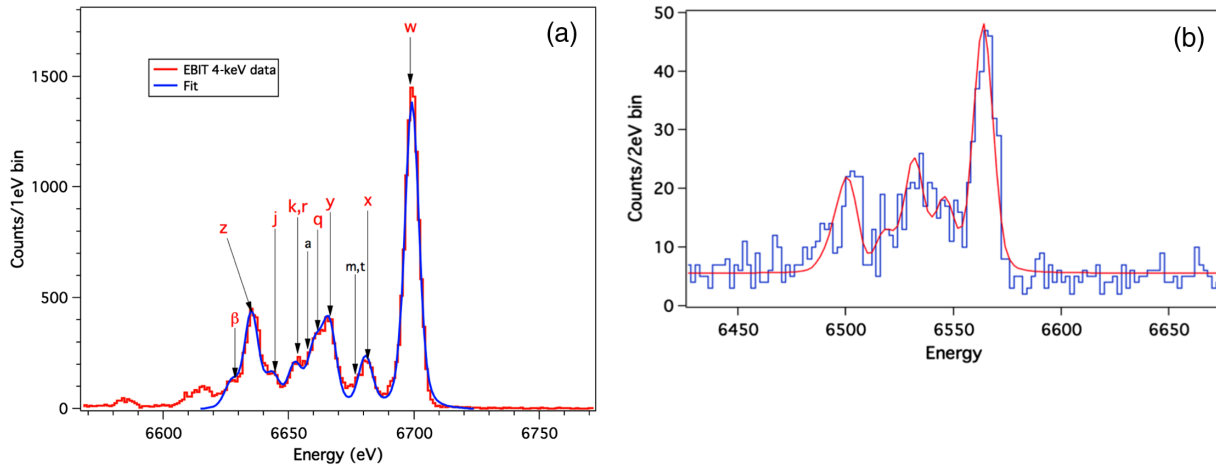


Fig. 3 (a) Empirical fit to calorimeter spectrum of laboratory plasma created at LLNL EBIT facility using a series of Gaussian lines. (b) Similar empirical fit to time slice of single pixel spectrum of Perseus. This method can be used to measure the residual differential gain drift for each pixel as a function of time.

Gaussian lines to the Fe xxv complex. The number of time slices for which the differential gain drift can be measured is limited by the statistical quality of the data. In Fig. 3(a), we show an example of fitting an empirical model to laboratory data³³ acquired with a calorimeter³⁴ at the Lawrence Livermore National Laboratory (LLNL) Electron Beam Ion Trap (EBIT) facility.^{35–39} This laboratory spectrum is very similar to the Fe K spectrum observed in Perseus. In Fig. 3(b), we show the same type of model being fit to data from a time slice of a single pixel in the observations of Perseus, resulting in a measurement of the differential gain drift for that pixel and time slice.

In Fig. 4(a), we show the results of fitting four time slices from two Perseus observations for three representative pixels in the main array. Both of the observations had the same aim-point, and during each observation, the pointing was stable to a fraction of a pixel; therefore, each pixel measures a constant spectrum over these two observations, and the data can be used to track differential gain drift. We plot these measurements as a function of the calibration pixel gain drift and fit them with a linear function. This reflects the reasonable but significant assumption that the common mode and differential gain drift have a related origin (although not necessarily a common

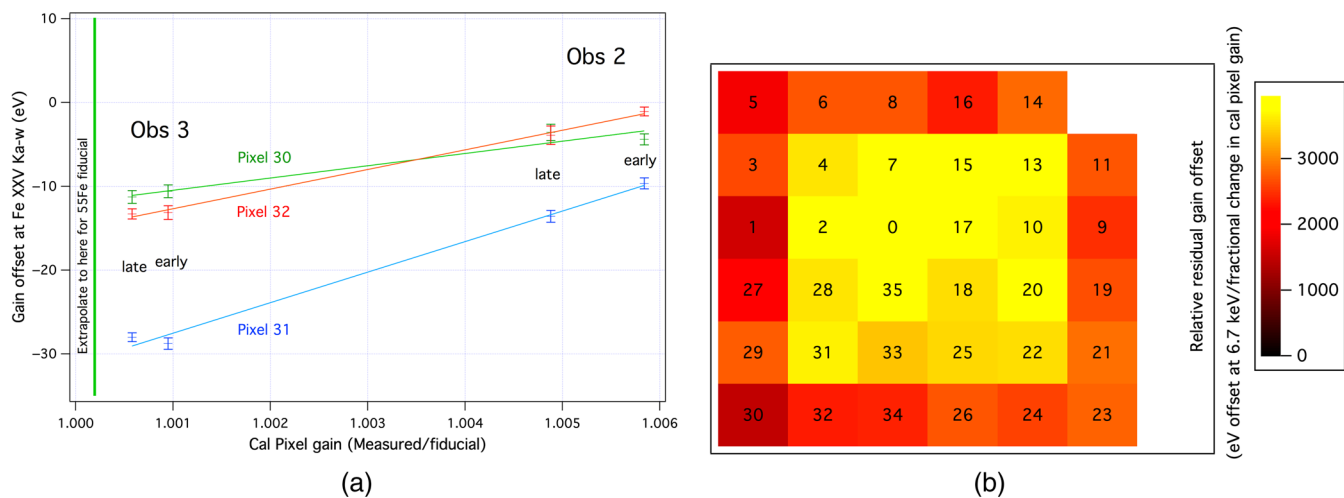


Fig. 4 (a) Residual differential gain drift for three representative pixels (30, 31, and 32) measured with fits to the Fe xxv spectrum of Perseus cluster in observations 2 and 3, each subdivided into early and late parts, plotted as a function of calibration pixel gain, which is used as a proxy for distance from thermal equilibrium. Data for all 35 array pixels (of which only three are shown) are fit to obtain the slope, which describes the relative differential gain drift as a function of calibration pixel gain drift. Note that the y-axis is a “relative” differential gain drift and does not include information from the ^{55}Fe fiducial measurement shown in Fig. 5. (b) Pixel map of slopes (energy offset per change in calibration pixel gain) obtained from the fits in panel (a). The central pixels show steeper slopes, while edge and corner pixels show shallower slopes. The residual differential gain term arises because the common-mode term in the gain is partially cancelled by a correlated radiative load; the central pixels show the strongest differential effect with respect to the calibration pixel gain because they have the weakest radiative load, while the calibration pixel has the strongest radiative load. The integers in the centers of pixels are the pixel numbers, which are arbitrary with respect to position in the array; however, the map does depict the true orientation of the pixels and their gain offsets.

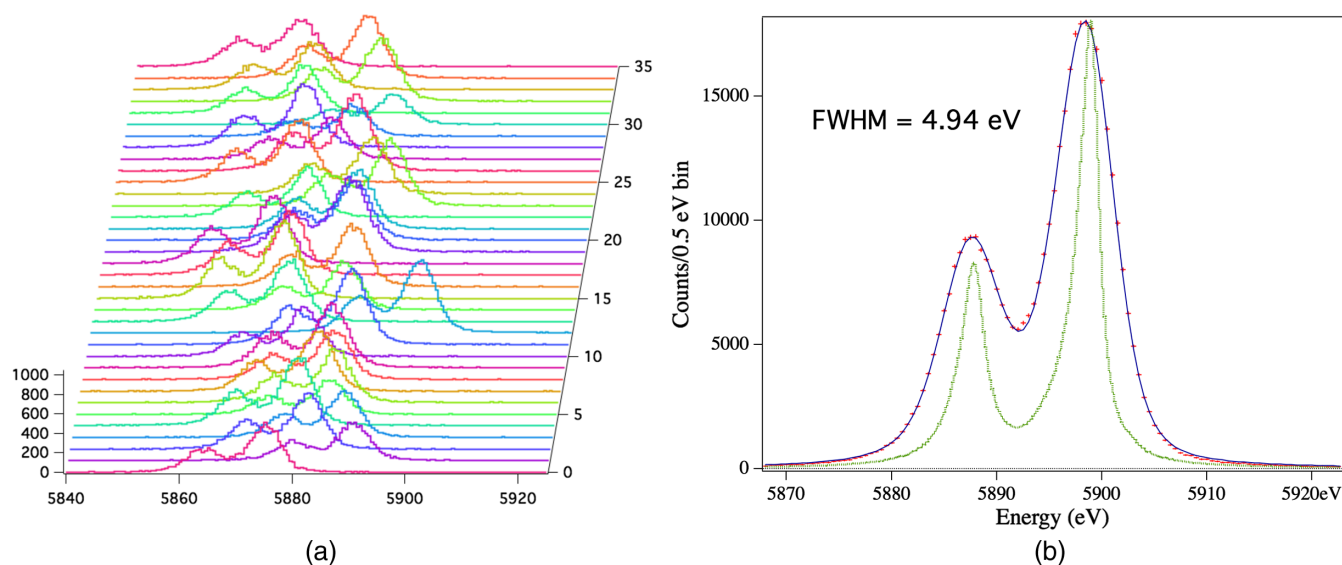


Fig. 5 (a) Waterfall diagram showing gain offset for each pixel after correction for the calibration pixel offset. Measurement of the offsets fixes the absolute offset of the gain scale at a single point in time and can be used to fix the intercept of the linear fits in Fig. 4(a). (b) Composite ^{55}Fe spectrum after correcting for the differential offset between pixels.

mechanism). The slope for each pixel gives the magnitude of the differential sensitivity of each pixel. In Fig. 4(b), we show a map of this differential sensitivity. The pattern of sensitivity shows that the gain changes in the innermost pixels are more different from the calibration pixel than the outer ring of pixels.

A difference in behavior between inner and outer pixels arises in differential loading from microwave radiation resonating in the CTS cavity, since the HgTe x-ray absorbers of the inner pixels are most shielded from absorption of microwave radiation due to their proximity to four neighboring absorbers; the edge and corner pixels are less shielded, with two or three neighbors; and the calibration pixel is the least shielded, with one neighbor. (The neighbor of the calibration pixel is an unwired alternate calibration pixel.) The radiative loading elevates the true temperature of the pixels with respect to the heat sink, and this effect is strongest in the earliest part of the mission and decreases as the dewar shields cool. In contrast, the common heat sink for all the pixels is depressed during the early parts of the mission because the conductive heat load from the helium tank onto the CTS control thermometer is greater. Thus, these two effects partially cancel in all pixels as the dewar cools, with the common-mode term dominating. The partial cancellation is strongest in the calibration pixel, and it thus shows the smallest gain variations. When the calibration pixel gain is used to correct the array pixel gains, it is an undercorrection, and the magnitude of the undercorrection is largest for the inner pixels, which experience the smallest radiative load and, thus, have the smallest cancellation of the common-mode term by the radiative term.

The slopes derived from the fits, as shown in Fig. 4(a), show the relative differential gain drift per pixel as a function of calibration pixel gain, but because the mean centroid per pixel of the Perseus spectrum is not known *a priori*, it cannot provide an absolute energy scale calibration. In other words, this figure allows us to measure the slope but not the intercept of the differential gain drift. The filter wheel was rotated to illuminate the full array with a radioactive ^{55}Fe source after all of the Perseus observations were completed, around the time that the SXS

dewar was coming into thermal equilibrium. This measurement of a line at a known energy allows us to fix the intercept of the linear functions as shown in Fig. 4(a) at the green line, which indicates the calibration pixel gain shift at the time of the ^{55}Fe filter wheel experiment. Figure 5(a) shows the Mn $K\alpha$ spectra from each pixel after correcting for the calibration pixel gain drift. Figure 5(b) shows the composite Mn $K\alpha$ spectrum after applying the offsets derived from this experiment.

In Fig. 6, we show the stacked spectrum from coadding all pixels in two observations of the Perseus cluster. The event energies have been corrected using the method described above. The broadening is slightly larger in the earlier observation than in the later one because of greater uncertainty in the extrapolation of the differential gain drift correction from the fiducial ^{55}Fe experiment, which occurred only a short time after the later observation.

In summary, our gain correction method implements the following steps: (1) we apply the ground gain calibration curves to every pixel to obtain a preliminary energy from the telemetered pulse heights, (2) we apply a time-dependent linear gain correction to all pixels (the “common-mode” correction), and (3) we apply a second time-dependent linear gain correction to each pixel, this time on a per-pixel basis (the “differential-mode” correction), based on the apparent relative drift rates of the fiducial lines on the array and on the cal pixel.

We note that the differential gain drift method described here is essentially the same as that used to measure the bulk velocity field in the Perseus cluster, as reported by the Hitomi collaboration (2016).⁴⁰ The turbulent velocity measurements reported in that article were performed using a different method, in which the drift for each pixel was corrected relative only to itself, destroying the bulk velocity information, but preserving the broadening.

In pipeline processing, this differential gain drift method was implemented in the task `sxsperseus`, which was used for data from observations 1 and 2. Observations 3 and 4 were much closer to thermal equilibrium, and thus, the standard gain scale software task was used.

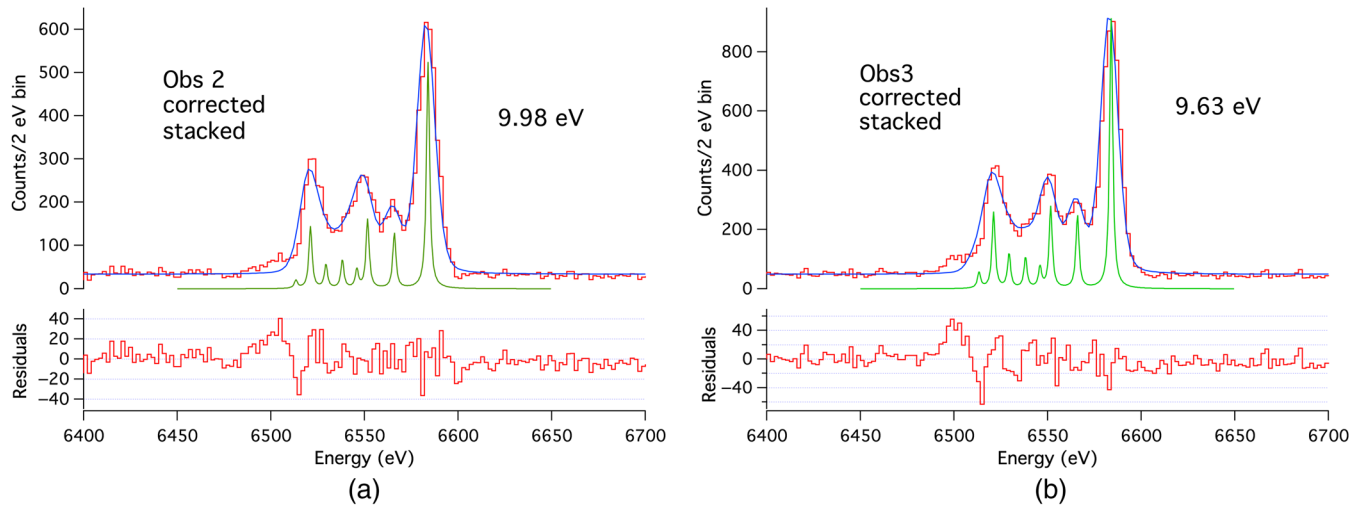


Fig. 6 Stacked spectrum from all pixels in observations 2(a) and 3(b) of Perseus after differential gain drift correction is applied. The broadening in each spectrum is dominated by the source linewidth (which includes the bulk velocity shear across the field of view), and it is expected to be the same for each observation. Observation 2 is slightly broader because of greater uncertainty in the extrapolation of the differential gain drift correction to earlier times in the mission. The 1σ statistical uncertainty on each measurement is 0.15 eV.

4 Effective Area

The instrument effective area contains contributions from the telescope (including thermal shield transmission), as well as the detector quantum efficiency and fill factor, and the dewar internal blocking filters. These quantities were all calibrated on the ground and are discussed in detail in several papers.^{18,19,21–25,41}

The dewar gate valve was kept closed to protect the dewar internal filters from potential contamination by outgassing material. This gate valve consists of a nominally 300- μm -thick beryllium window covered by a 0.2-mm-thick stainless steel mesh with 71% open fraction.

Because of the early termination of mission operations, all of the observations were conducted before the gate valve was opened. Furthermore, because the early observations were intended to evaluate the instrument and observatory capabilities and not to perform key science observations, the transmission of the gate valve was not directly measured preflight but was instead estimated using the midpoint of the manufacturer’s quoted measurement of the beryllium thickness of 274 to 290 μm .⁴²

To extract the maximum science output from the limited number of observations performed, a better estimate of the beryllium window thickness is required. We estimated the window thickness in two ways: first, we fit the observed spectra of two bright astrophysical continuum sources, and second, we measured the x-ray transmission of the flight spare gate-valve beryllium window using a beamline at the SPring8 synchrotron. The flight spare window is expected to be identical to the flight window.

We jointly modeled the observed spectra of two bright continuum sources, the Crab nebula and G21.5-0.9, using a model with beryllium thickness as a free parameter. The derived thickness is $270 \pm 10 \mu\text{m}$ (statistical). We estimate that a 10- μm systematic error may be introduced by our ad-hoc method of modeling the electron loss continuum in this procedure.

The SPring8 measurements are reported by Hoshino et al.⁴³ The best-fit beryllium thickness is $261.86 \pm 0.01 \mu\text{m}$. Edges

due to contaminants are detected and included in the model; these include Ni, Fe, Cu, Mn, and Cr. Other weak edge-like features were also detected, which are interpreted as being due to Bragg diffraction from polycrystalline beryllium.

The synchrotron measurements of the spare beryllium window are much more precise than the modeling of the window thickness from spectra of astrophysical calibration targets. Therefore, we adopt a model based on the synchrotron measurements in our final calibration data file for the gate-valve beryllium window.¹⁸ The good agreement of the astrophysical calibration spectral fits with the laboratory measurements validates the model to the extent possible.

Because of the presence of the SXS gate valve in all observations, the validity of the gate-valve-open effective area model at low energies could not be tested in flight. The verification of the high-energy effective area model will be discussed in a future article.

5 Timing

For each event, the photon arrival time is calculated from the event trigger time or pulse derivative maximum time. However, the method of determination of the trigger and derivative maximum times is different among event grades, leading to systematic differences that must be calibrated.

The preflight modeling of the pulse timing assumed a time assignment of the form⁶

$$\text{SAMPLECNT} = \text{SAMPLECNTTRIG} - a \frac{\text{RISE_TIME}}{4} - b \text{DERIV_MAX} - c. \quad (6)$$

In the above equation, SAMPLECNTTRIG is the photon arrival time calculated by the PSP, while SAMPLECNT is the corrected, “true” photon arrival time calculated in postprocessing on the ground. RISE_TIME is the event rise time calculated by the PSP, and DERIV_MAX is the pulse derivative maximum time calculated by the PSP. The parameters a , b , and c are

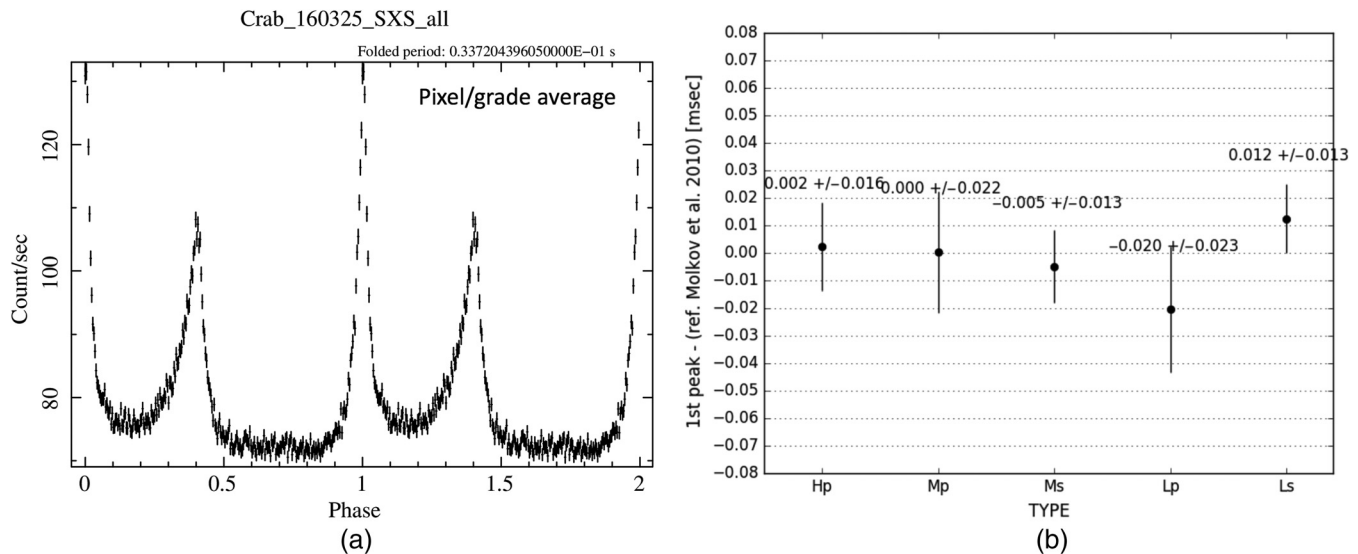


Fig. 7 (a) Phase folded pulse profile of the Crab nebula. Fits to the first peak centroid were used to refine the timing parameters by pixel and event grade. (b) Resulting peak offset relative to expected peak position (based on radio ephemeris) as a function of event grade.

defined for each event grade grouping: hi-res, mid-res, and low-res, respectively.

In preflight modeling,⁴⁴ a and b were not expected to be large and were, thus, assumed to be zero for all pixels and event grades. c was found to be 1.625 for hi-res and mid-res graded events on pixel 26, and zero for hi-res and mid-res graded events on all other pixels. The difference in c for pixel 26 is because it had a higher trigger threshold setting when its pulse template was created due to ringing behavior,⁶ resulting in a shifted event trigger time. For low-res graded events, c was found to be 11.625.

The timing of the events was evaluated using an observation of the Crab nebula. Its pulse profile is shown in Fig. 7(a). The folding parameters (P , \dot{P} , and T_0) were calculated using a simultaneous radio observation.⁴⁵

Because RISE_TIME and DERIV_MAX are correlated, and the distribution of RISE_TIME relative to DERIV_MAX is narrow, a was kept at zero, and b and c were evaluated as follows.

For each event grade grouping (hi-res, mid-res, and low-res), events were split into three DERIV_MAX bins (100 to 2600, 2600 to 5100, and 5100 to 7600). For each DERIV_MAX bin, a folded light curve was constructed, and the first pulse peak was fit with a Gaussian model to find the timing centroid. The b coefficient was evaluated by performing a linear fit to the relative time shift as a function of DERIV_MAX. The b coefficient is small for all event grades, and the statistical constraints on it are not strong.

After correcting the event time with the b coefficient, corrections to the c coefficients were evaluated by fitting the first pulse peak for each event grouping (hi-res, mid-res, and low-res) and comparing the best-fit peak centroid to that predicted using a contemporary high precision radio ephemeris⁴⁵ together with the 3- to 20-keV x-ray phase lag relative to the radio peak measured by Molkov et al.⁴⁶ The results of this procedure are shown in Fig. 7(b). The relative event-to-event timing is validated at the 20- μ s level, while the absolute timing accuracy is estimated to be at the 100- μ s level, with contributions from systematic uncertainty in the radio ephemeris by Molkov et al.,⁴⁶ as well as statistical and systematic uncertainties in the radio ephemeris by

Terada et al.⁴⁵ We note that the relative pixel-to-pixel timing accuracy is independently confirmed with a similar level of precision by studies of coincident events due to cosmic rays in the pixels and anticoincidence detector.

6 Summary

Although the SXS was not able to finish the full planned suite of in-flight calibration measurements, its expected performance was confirmed. The array-averaged energy resolution was better than 5-eV full width at half maximum at 5.9 keV despite moderate electrical interference from the AOCS. The energy scale was reconstructed to high accuracy for early observations of the Perseus cluster performed during the SXS commissioning phase, even in the absence of regular measurements of calibration fiducials, allowing a measurement of the bulk velocity field in Perseus.⁴⁰ The outstanding performance of the SXS combined with the high quality of the calibration achieved even in a very limited campaign is a strong indication of the promise of x-ray calorimeter spectrometer technology for future x-ray observatories.

Acknowledgments

We thank all of the US, Japanese, and European SXS team members who contributed to the years of development and testing at GSFC, Niihama, Tsukuba, and Tanegashima, including the postdocs and students who supported the long series of tests at Niihama and Tsukuba. Part of this work was performed under the auspices of the US DoE by LLNL under Contract No. DE-AC52-07NA27344 and also supported by NASA grants to LLNL.

References

1. T. Takahashi et al., “The ASTRO-H (Hitomi) X-ray Astronomy Satellite,” *J. Astron. Telesc. Instrum. Syst.* 4(2) 021402 (2018).
2. R. L. Kelley et al., “The ASTRO-H High Resolution Soft X-ray Spectrometer,” *J. Astron. Telesc. Instrum. Syst.*, submitted (2018).
3. F. S. Porter et al., “In-flight performance of the Soft X-ray Spectrometer detector system on ASTRO-H,” *J. Astron. Telesc. Instrum. Syst.* 4(2), 011218 (2018).

4. C. A. Kilbourne et al., “The design, implementation, and performance of the ASTRO-H SXS calorimeter array and anti-coincidence detector,” *J. Astron. Telesc. Instrum. Syst.* **4**(2), 011215 (2018).
5. M. P. Chiao et al., “System design and implementation of the detector assembly of the Astro-H Soft X-ray Spectrometer,” *J. Astron. Telesc. Instrum. Syst.*, submitted (2018).
6. Y. Ishisaki et al., “In-flight performance of pulse processing system of the ASTRO-H/Hitomi Soft X-ray Spectrometer,” *J. Astron. Telesc. Instrum. Syst.* **4**(2), 011217 (2018).
7. C. K. Kilbourne et al., “The design, implementation, and performance of the Astro-H SXS aperture assembly and blocking filters,” *J. Astron. Telesc. Instrum. Syst.* **4**(2), 011215 (2018).
8. G. A. Sneiderman et al., “Cryogen-free operation of the Soft X-ray Spectrometer instrument,” *J. Astron. Telesc. Instrum. Syst.*, submitted (2018).
9. P. J. Shirron et al., “Design and on-orbit operation of the Soft X-ray Spectrometer ADR on the Hitomi Observatory,” *J. Astron. Telesc. Instrum. Syst.* **4**(2), 021403 (2018).
10. Y. Ezoe et al., “Porous plug phase separator and superfluid film flow suppression system for the Soft X-ray Spectrometer onboard Hitomi,” *J. Astron. Telesc. Instrum. Syst.* **4**(2), 011203 (2017).
11. H. Noda et al., “Thermal analyses for initial operations of the Soft X-ray Spectrometer onboard the Hitomi satellite,” *J. Astron. Telesc. Instrum. Syst.* **4**, 011202 (2017).
12. R. Fujimoto et al., “Performance of the helium dewar and cryocoolers of the Hitomi Soft X-ray Spectrometer,” *J. Astron. Telesc. Instrum. Syst.* **4**(2), 011208 (2017).
13. Y. Takei et al., “Vibration isolation system for cryocoolers of Soft X-ray Spectrometer (SXS) onboard ASTRO-H (Hitomi),” *J. Astron. Telesc. Instrum. Syst.* **4**(2) 011216 (2018).
14. T. Sato et al., “Examining the angular resolution of the ASTRO-H’s Soft X-ray Telescopes,” *J. Astron. Telesc. Instrum. Syst.* **2**, 044001 (2016).
15. T. Okajima et al., “First peek of ASTRO-H Soft X-ray Telescope (SXT) in-orbit performance,” *Proc. SPIE* **9905**, 99050Z (2016).
16. M. Tsujimoto et al., “In-orbit operation of the Soft X-ray Spectrometer onboard the Hitomi satellite,” *J. Astron. Telesc. Instrum. Syst.* **4**(2), 011205 (2017).
17. L. Angelini et al., “Astro-H/Hitomi data analysis, processing and archive,” *J. Astron. Telesc. Instrum. Syst.* **4**(2), 011207 (2018).
18. M. E. Eckart et al., “Ground calibration of the ASTRO-H (Hitomi) Soft x-ray Spectrometer,” *J. Astron. Telesc. Instrum. Syst.*, submitted (2018).
19. T. Sato et al., “Revealing a detailed performance of the Soft X-ray Telescopes of the ASTRO-H mission,” *Proc. SPIE* **9144**, 914459 (2014).
20. N. Kikuchi et al., “Atomic scattering factor of the ASTRO-H (Hitomi) SXT reflector around the gold’s L edges,” *Opt. Express* **24**, 25548 (2016).
21. S. Kurashima et al., “Reflectivity around the gold M-edges of x-ray reflector of the Soft X-ray Telescope onboard ASTRO-H,” *Proc. SPIE* **9905**, 99053Y (2016).
22. Y. Maeda et al., “Reflectivity around the gold L-edges of x-ray reflector of the Soft X-ray Telescope onboard ASTRO-H,” *Proc. SPIE* **9905**, 99053Z (2016).
23. T. Sato et al., “The ASTRO-H SXT performance to the large off-set angles,” *Proc. SPIE* **9905**, 99053X, (2016).
24. T. Hayashi et al., “Point spread function of ASTRO-H Soft X-ray Telescope (SXT),” *Proc. SPIE* **9905**, 99055D (2016).
25. R. Iizuka et al., “Ground-based x-ray calibration of the Astro-H/Hitomi Soft X-ray Telescopes,” *J. Astron. Telesc. Instrum. Syst.* **4**(2), 011213 (2018).
26. M. A. Leutenegger et al., “In-flight calibration of Hitomi Soft X-ray Spectrometer (5) line spread function,” *Publ. Astron. Soc. Jpn.*, in preparation.
27. M. E. Eckart et al., “In-flight calibration of Hitomi Soft X-ray Spectrometer (4) gain scale,” *Publ. Astron. Soc. Jpn.*, in preparation.
28. M. Tsujimoto et al., “In-flight calibration of Hitomi Soft X-ray Spectrometer (3) effective area,” *Publ. Astron. Soc. Jpn.*, in press.
29. S. Koyama et al., “In-orbit timing calibration of SXS, HXI and SGD on board Hitomi,” *Publ. Astron. Soc. Jpn.*, in preparation.
30. C. A. Kilbourne et al., “In-flight calibration of Hitomi Soft X-ray Spectrometer (1) background,” *Publ. Astron. Soc. Jpn.*, in press.
31. Y. Maeda et al., “Inflight calibration of the Hitomi Soft X-ray Spectrometer (2) point spread function,” *Publ. Astron. Soc. Jpn.*, in press.
32. F. S. Porter et al., “Temporal gain correction for x-ray calorimeter spectrometers,” *J. Low Temp. Phys.* **184**, 498–504 (2016).
33. M. F. Gu et al., “Laboratory measurements of the dielectronic recombination satellite transitions of He-like Fe XXV and H-like Fe XXVI,” *Can. J. Phys.* **90**, 351–357 (2012).
34. F. S. Porter et al., “The Astro-E2 X-ray spectrometer/EBIT microcalorimeter x-ray spectrometer,” *Rev. Sci. Instrum.* **75**, 3772–3774 (2004).
35. R. E. Marrs et al., “Measurement of electron-impact-excitation cross sections for very highly charged ions,” *Phys. Rev. Lett.* **60**, 1715–1718 (1988).
36. R. E. Marrs, P. Beiersdorfer, and D. Schneider, “The electron-beam ion trap,” *Phys. Today* **47**(10), 27–34 (1994).
37. P. Beiersdorfer, “Laboratory x-ray astrophysics,” *Annu. Rev. Astron. Astrophys.* **41**, 343–390 (2003).
38. R. E. Marrs, “Milestones in EBIT spectroscopy and why it almost did not work,” *Can. J. Phys.* **86**, 11–18 (2008).
39. G. V. Brown et al., “A brief overview of the fusion and astrophysics data and diagnostic calibration facility,” *Proc. SPIE* **7732**, 77324Q (2010).
40. F. Aharonian et al., “The quiescent intracluster medium in the core of the Perseus cluster,” *Nature* **535**, 117–121 (2016).
41. Y. Soong et al., “ASTRO-H Soft X-ray Telescope (SXT),” *Proc. SPIE* **9144**, 914428 (2014).
42. M. E. Eckart et al., “Ground calibration of the ASTRO-H (Hitomi) Soft x-ray Spectrometer,” *Proc. SPIE* **9905**, 99053W (2016).
43. A. Hoshino et al., “The evaluation of the Hitomi (Astro-H)/SXS spare beryllium window in 3.8–30 keV,” *Proc. SPIE* **10397**, 103970E (2017).
44. M. Tashiro et al., “SXS timing coefficients,” 2016, http://heasarc.gsfc.nasa.gov/docs/hitomi/calib/caldb_doc/asth_sxs_caldb_coef_v20160310.pdf
45. Y. Terada et al., “X-ray studies of Giant Radio Pulses from Crab pulsar with Hitomi,” *Publ. Astron. Soc. Jpn.* in press.
46. S. Molokov, E. Jourdain, and J. P. Roques, “Absolute timing of the crab pulsar with the INTEGRAL/SPI telescope,” *Astrophys. J.* **708**, 403–410 (2010).

Biographies for the authors are not available.